INTERNATIONAL JOURNAL FOR NUMERICAL METHODS IN FLUIDS, VOL. 24, 893–912 (1997)

NUMERICAL STABILITY ANALYSIS FOR FREE SURFACE FLOWS

MINGLUN WANG[1] AND ARMIN W. TROESCH[2]*

[1] *American Bureau of Shipping New York, New York, NY, U.S.A.*
[2] *Department of Naval Architecture and Marine Engineering, The University of Michigan, Ann Arbor, MI 48109, U.S.A.*

SUMMARY

A systematic methodology of numerical stability is presented here in the study of numerical properties of mixed Eulerian–Lagrangian schemes for the numerical simulation of non-linear free surface flows. Two different numerical schemes, i.e. a source–doublet panel method and a desingularized method, are investigated. The present work provides theoretical foundations and applications for numerical stability analysis theory. The matrix stability method has been developed to obtain the spectral radii and normal modes associated with free surface discretization. Some examples considered illustrate the usefulness of this analysis. © 1997 by John Wiley & Sons, Ltd. Int. j. numer. methods fluids 24: 893–912, 1997.

(No. of Figures: 15. No. of Tables: 1. No. of Refs: 17.)

KEY WORDS: numerical stability; mixed Eulerian–Lagrangian scheme; free surface flow

1. INTRODUCTION

Until recently, numerical methods for solving non-linear free surface flows have been dominated by mixed Eulerian–Lagrangian formulations. These powerful methods, which play a major role in free surface calculations, raise the stability issue owing to the discrete representation of free surface elevation. In this study we present fundamental advances and insights into these methods and discuss various numerical stability theories.

Ever since Longuet-Higgins and Cokelet[1] encountered saw-tooth instabilities in their initial application, numerical stability has gradually become a significant concern to investigators using the mixed Eulerian–Lagrangian scheme with free surface problems. Numerical techniques such as regriding, smoothing, filtering and artificial damping have been adopted by analysis and intuition to surmount or reduce the instability. Several methods based on Fourier analysis have been developed and applied. The principal methods include the popular von Neumann analysis,[2] spectral analysis[3] based upon the discrete dispersion relation obtained from the Fourier transform, and the matrix method.[4] Yeung[2] and Dommermuth *et al.*[5] applied a von Neumann analysis to give the stability criteria $f = kg\Delta t^2/2$ and $\Delta t^2 \leqslant (8/\pi)\Delta x/g$ respectively. Here Δt and Δx represent time step and

* Correspondence to: A. W. Troesch, Department of Naval Architecture and Marine Engineering, The University of Michigan, Ann Arbor, MI 48109, U.S.A.

Contract grant sponsor: Office of Naval Research United States Navy; Contract grant numbers: DOD-G-N00014-90-J-1818, DOD-G-N00014-94-1-0652, DOD-G-N00014-96-1-0482

CCC 0271–2091/97/090893–20$17.50 *Received 1 September 1996*

mesh size respectively and g is gravitational acceleration. This approach assumed a particular relationship between free surface normal velocities and velocity potentials based upon linear water gravity waves, i.e. $\phi_z = k\phi$. Nakos *et al.*[6] extended the spectral analysis method[3] to a transient free surface flow around a constant Rankine source with a uniform speed. The comparison of the discrete and continuous dispersion relations gave a systematic global error and stability criteria. Also included in that work was the effect on stability due to an artificial absorption zone. Park and Troesch[4] developed a matrix method to investigate the stability effects due to different numerical schemes, far-field closure and Green's function constant, thus proposing the free surface stability (FSS) number given by $FSS = \pi g \Delta t^2 / \Delta x$. Park and Troesch[4] also provided a comprehensive stability analysis with various applications.

This paper extends the last model[4] to investigate different mixed Eulerian–Lagrangian schemes, such as Cao's DBEM (desingularized boundary element methods)[7–9] and Maskew's USAERO/FSP,[10] as well as the effect of an artificial absorption device. The matrix method described in Reference 4 is further developed to analyse the spectral radii and normal modes of the free surface discretization used in developing the stability criteria, as well as to evaluate the effects of the desingularized distance in the DBEM and the influence of artificial absorption zones. Additional details and examples can be found in Reference 11.

It is noted that the stability analyses presented here are linearized theories which cannot fully answer the non-linear free surface stability problems. This study, however, demonstrates that a linear numerical stability analysis is useful for designing efficient and robust non-linear schemes.

2. THE MIXED EULERIAN–LAGRANGIAN SCHEME

Under the circumstances that we can justify the mathematical simplification and approximations, e.g. constant fluid density, negligible viscous effects and no vorticity, the velocity field is represented simply as the gradient of a scalar function, i.e. the velocity potential or $\mathbf{u}(\mathbf{x}, t) = \nabla\phi(\mathbf{x}, t)$. The bold character $\mathbf{x} = (x, y, z)$ signifies the field vector with three co-ordinate components and hence the irrotational flow of an incompressible, inviscid fluid is governed by the Laplace equation. An earth-bound Cartesian co-ordinate system Oxyz is defined with its origin on the still water surface and its z-axis pointing upwards.

The boundary element method is claimed to have a speed and resolution advantage over finite difference and classical finite element methods. These perceived advantages have led many investigators to use the mixed Eulerian–Lagrangian scheme developed by Longuet-Higgins and Cokelet[1] when solving non-linear free surface problems. Longuet-Higgins and Cokelet[1] derived a two-step solution procedure divided into a Eulerian boundary element method (BEM) and a Lagrangian finite difference scheme. The first step addresses a boundary value problem in the Eulerian zone to obtain the velocity on the free surface, where the velocity potential and the co-ordinates of marked particles at the free surface are provided at the previous time step. Then the second step updates the velocity potential and the free surface by integrating the Lagrangian formulations for the dynamic and kinematic free surface boundary conditions.

The boundary element method can be viewed as a singularity distribution method by performing the following steps: first distribute some type of discretized singularities over some surface S_s, called the integration surface, around the boundaries of the fluid domain; then select a set of collocation points, usually the same as the number of degrees of freedom of the singularity distribution, on the boundaries S_c, called the control surface; describe the boundary conditions at these collocation points in the unknown strength of singularities; and finally solve the resulting closed set of equations for the unknown strength, thus determining the potential and velocity everywhere in the domain.

2.1. Desingularized source distribution

We first consider the desingularized method. Different from conventional BEM methods, the desingularized boundary element method separates the integration and control surfaces with a proper desingularized distance so that the singularities migrate outside the fluid domain and the collocation points remain on the boundaries. Therefore the singularities and the collocation points no longer coincide, which results in non-singular formulations. See Figure 1 for an example of tank sloshing.

Applying Green's second identity to the velocity potential satisfying the Laplace equation yields a Fredholm integral equation represented by

$$\phi(P) = -\int_{S_s} \left(\phi(Q) \frac{\partial G(P, Q)}{\partial n} - G(P, Q) \frac{\partial \phi(Q)}{\partial n} \right) \mathrm{d}s, \tag{1}$$

where $G(P, Q)$ is the Green function, P is the field point with co-ordinates $\mathbf{x}_P = (x, y, z)$ on the control surface and Q is the singularity point with co-ordinates $\mathbf{x}_Q = (\xi, \eta, \zeta)$ on the integration surface.[12,13] If all the boundary conditions are well posed, the uniqueness of the solution to the integral equation is guaranteed.

Extending the domain Ω into $\Omega \cup \Omega_e$ and letting $\phi = \phi_e$ and $\sigma(Q) = \phi_{\mathbf{n}} - \phi_{e_{\mathbf{n}}}$ produces another integral equation expressed as

$$\phi(P) = \int_{S_s} \sigma(Q) G(P, Q) \, \mathrm{d}s, \tag{2}$$

where $\sigma(Q)$ is the unknown strength of sources, which is determined by the boundary conditions. Any solution to the Poisson equation $\Delta\phi = \delta(P, Q)$ can serve as the Green function $G(P, Q)$. Both Dirichlet and Neumann boundary conditions can be imposed upon equation (2). The solution procedure is implemented numerically by discretizing the above equations, resulting in

$$\phi_{\mathscr{D}}(P_j) \approx \sum_{i=1}^{N_{\mathscr{D}}} \sigma(Q_i) G(P_j, Q_i) \quad \text{on } \Gamma_{\mathscr{D}} \quad \text{for } j = 1, \ldots, N_{\mathscr{D}}, \tag{3}$$

$$\frac{\partial \phi_{\mathscr{N}}(P_j)}{\partial \mathbf{n}} \approx \sum_{i=1}^{N_{\mathscr{D}}} \sigma(Q_i) \frac{\partial G(P_j, Q_i)}{\partial \mathbf{n}} \quad \text{on } \Gamma_{\mathscr{N}} \quad \text{for } j = 1, \ldots, N_{\mathscr{N}}, \tag{4}$$

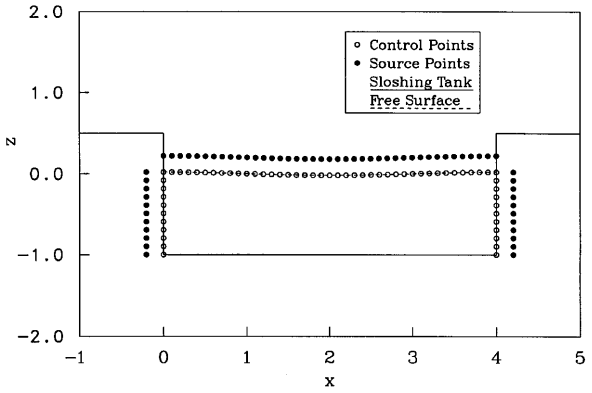

Figure 1. Source and control point distribution for sloshing tank, where bottom condition is satisfied by using image sources

where $N_{\mathscr{D}}$ and $N_{\mathscr{N}}$ are the numbers of collocation points on the Dirichlet and Neumann boundaries respectively.

Cao[7] suggested that the desingularization distance should be given by

$$d = l_{\mathrm{d}} \Delta x^{v}, \tag{5}$$

where l_{d} is the desingularization factor reflecting the extent of desingularization, v is a parameter that affects the accuracy of the numerical integration and Δx is the local mesh size. His numerical experiments[7,8] showed that an appropriate value for v lies between 0 and 1 and a good choice for the desingularization is $v = \frac{1}{2}$. Cao[7] also pointed out that the limit of the non-singular formulation is consistent with the singular one and the desingularized integral equation is expected to have similar properties to the singular integral equation.

An issue separate from stability considerations of the DBEM is matrix conditioning. Since in this method the integral kernels are now non-singular, some degree of diagonal dominance has been lost, yielding less well-conditioned matrices. Cao *et al.*[8] have calculated a representative matrix condition number as a function of the desingularized distance. The reader is referred to that work for a more complete discussion.

2.2. Source and doublet singularity distribution

The source–doublet panel method is a three-dimensional non-linear time-stepping scheme developed by Maskew[10] for free surface problems associated with arbitrary multiple bodies in general motion. This time-stepping surface singularity adopts quadrilateral panels by uniformly distributing both source and doublet singularities on boundary surfaces of the problem. The surface integrals in Green's theorem are evaluated in a piecewise manner over each panel to form panel influence coefficients. These evaluations are performed for each panel acting at the central control points on all the surface panels, thus forming a matrix of influence coefficients. Usually the strengths of the sources are determined by the local velocity components normal to the panel surfaces at the start of each time step and then the strengths of the doublet are solved from the matrix equations. There is also a provision to solve for the strengths of the sources when the strengths of the doublets are given. Thus mixed boundary condition problems can also be treated.

Here we adopt the convention used in Reference 10. The fluid velocity $\mathbf{V}$ is the negative gradient of the potential, i.e. $\mathbf{V} = -\nabla\Phi$. In USAERO/FSP, all variables are normalized by certain reference quantities; see Reference 10 for details. Different from the desingularized method, both source and doublet singularities are directly distributed over the boundary surfaces of the fluid domain. We have a singular point when the field point P coincides with the source and doublet point Q. The limiting process as the singular point approaches a smooth boundary produces the local contribution $\phi(P)/2$, thus yielding

$$\sum_{k=1}^{N_{\mathrm{b}}} \mu_k C_{jk} + \sum_{k=1+N_{\mathrm{b}}}^{N} \sigma_k B_{jk} + E_{jk} = 0 \quad \text{for } j = 1, \ldots, N. \tag{6}$$

On non-smooth boundaries the local contribution to $\phi(P)$ is not scaled by $\frac{1}{2}$ but rather by the internal angle divided by 2π or 4π depending upon whether the problem is two-dimensional or three-dimensional. In this work, however, we exclude corners or non-smooth boundaries from the set of singular points. It follows then for equation (6) that

$$C_{jj} = -2\pi, \qquad E_{jk} = \sum_{k=1}^{N_{\mathrm{b}}} \sigma_k B_{jk} + \sum_{k=1+N_{\mathrm{b}}}^{N} \mu_k C_{jk}$$

and μ_k and σ_k are the doublet and source densities respectively on panel k. N is the total number of active panels on all local wetted surfaces, including the free surface, N_f, and the hull configuration, N_b. C_{jk} and B_{jk} are the influence coefficients respectively for the uniform doublet and source on panel k acting at the control point of panel j. See Reference 14 for the formulae of C_{jk} and B_{jk}.

2.3. Artificial absorption devices

More recently, artificial absorption devices, which will be briefly described below, were contrived to implement far-field closure. For the wave propagation problems with an unbounded domain the computational domain has to be limited to a finite region by truncating the free surface at a certain distance. The imposition of appropriate radiation boundary conditions can greatly reduce wave reflections. An intuitive method for the imposition of radiation boundary conditions may be based on Sommerfeld's idea[15] which slightly modifies the problem by adding a small damping term.

Numerous artificial damping systems have been devised to attempt at improving the mixed Eulerian–Lagrangian scheme for free surface problems. Nakos *et al.*[6] presented two linearized types of artificial damping systems. However, their two models[6] are designed to *absorb* kinematic motion instead of energy. A stability analysis for their absorption device may also be found in Reference 6. Here we design an artificial energy absorption system for non-linear free surface models

$$\frac{\mathrm{D}\phi}{\mathrm{D}t} = -gz + \tfrac{1}{2}\nabla\phi\cdot\nabla\phi - \nu\phi_n, \qquad \frac{\mathrm{D}\mathbf{x}}{\mathrm{D}t} = \nabla\phi, \tag{7}$$

where, for convenience, $\nu(x)$ is non-negative and called the *Newtonian cooling* or *friction* coefficient.[16]

Israeli and Orszag[16] state that there exists an *optimum* value of the cooling strength for maximum wave absorption. We designed the absorption device defined by

$$\nu(x) = \begin{cases} 0, & 0 \leqslant x \leqslant x_0, \\ \nu_0\{1 - \cos[\pi(x - x_0)/(L - x_0)]\}, & x_0 < x \leqslant L, \end{cases} \tag{8}$$

where the cooling strength ν_0 is suggested to lie between 0·1 and 0·3 by numerical simulations. The stability analyses are given in Section 4.3.

3. NUMERICAL STABILITY THEORY

The stability concepts under discussion are properties of a particular linearized system that presumably represents a non-linear model of free surface problems in terms of physical variables of interest such as time step, mesh size, desingularized distance, damping coefficient and so on. The question of stability is concerned with the examination of error growth while a numerical scheme is being carried out. A basic issue involves the preservation of stability under a change in parameter values. Since transient parameters (e.g. those associated with non-linear systems) change with time, stability can be created or destroyed as the equations are integrated forwards. To circumvent the difficulty of a non-linear stability analysis, we must limit our attention to approximate linear models.

Historically, von Neumann stability analysis has served as a basic tool for stability studies. Early attempts at a stability criterion for the mixed Eulerian–Lagrangian scheme were largely based on this method. The method's chief attributes are its relative simplicity of implementation and its ability to estimate stability characteristics of individual surface elements. The von Neumann analysis, however, is only approximate since it does not include the effects of the boundaries. More recently the matrix method[4] and spectral analysis[6] have been developed to overcome this shortcoming. If influences such

as the effects of different boundary conditions on stability are desired, we are limited to the matrix method, which is briefly described in the following paragraphs.

For a linear stability analysis we have the linearized free surface boundary conditions

$$\eta_t = \phi_z \quad \text{and} \quad \phi_t = -g\eta \quad \text{on } z = 0. \tag{9}$$

Various difference approximations can be applied to the above equations. For instance, an explicit Euler scheme generates

$$\phi^{n+1} - 2\phi^n + \phi^{n-1} = -g\Delta t^2 \phi_z^{n-1}, \tag{10}$$

an implicit Euler scheme produces

$$\phi^{n+1} - 2\phi^n + \phi^{n-1} = -g\Delta t^2 \phi_z^{n+1} \tag{11}$$

and an E–I Euler scheme (implicit–explicit) yields

$$\phi^{n+1} - 2\phi^n + \phi^{n-1} = -g\Delta t^2 \phi_z^{n}. \tag{12}$$

For a simple case these above equations given by the three different schemes can be directly investigated by von Neumann stability analysis. For a survey of various difference schemes one may refer to Reference 2.

In general, assume a scheme to be of the form

$$C_1 f_j^{n+1} + C_0 f_j^n + C_{-1} f_j^{n-1} = 0, \tag{13}$$

where $C_i, i = -1, 0, 1$, are finite difference operators and $f_j^n \approx f(\mathbf{x}_j, t^n)$ are discrete variables described by the space discretization $\mathbf{x}_j$ and the time discretization $t^n = n\Delta t$, where n is the integer indicating the time step. A Fourier analysis of the solution to equation (13) provides the representation

$$f_j^n = F^n(\mathbf{k}) \mathrm{e}^{\mathrm{i}\mathbf{k} \cdot \mathbf{x}_j}, \tag{14}$$

where $i = \sqrt{(-1)}$ and $\mathbf{k}$ is the vector wave number. Substituting equation (14) into equation (13) and dividing by the factor $\exp(\mathrm{i}\mathbf{k} \cdot \mathbf{x}_j)$ yields the vector equation

$$G_1 F_j^{n+1} + G_0 F_j^n + G_{-1} F_j^{n-1} = 0. \tag{15}$$

This three-level equation can be transformed into a two-level equation by introducing the auxiliary unknown $U^n = F^{n-1}$. Then equation (15) becomes

$$G_1 F_j^{n+1} + G_0 F_j^n + G_{-1} U_j^n = 0, \qquad U_j^{n+1} - F_j^n = 0, \tag{16}$$

which can be combined into

$$\mathbf{\Phi}^{n+1} = \mathbf{G}\mathbf{\Phi}^n, \tag{17}$$

where $\mathbf{\Phi} = (\mathbf{F}, \mathbf{U})$ is a $2m$-component vector and $\mathbf{G}$ is a $2m \times 2m$ matrix consisting of the operators of equations (16).

Stability of the scheme requires that the spectral radius of the amplification matrix $\mathbf{G}$ be not larger than unity, i.e.

$$\rho(\mathbf{G}) = \max_i |\lambda_i| \leqslant 1, \quad 0 \leqslant k_j \Delta x_j \leqslant 2\pi, \tag{18}$$

where λ_i are the eigenvalues of $\mathbf{G}$. These eigenvalues are the roots of the algebraic equation

$$\det(\mathbf{G} - \lambda \mathbf{I}) = 0, \tag{19}$$

where $\mathbf{I}$ is the identity matrix.

For the mixed Eulerian–Lagrangian scheme the linearized free surface boundary conditions described by equations (9) can be represented in the discretization system

$$\begin{Bmatrix} \phi \\ \eta \end{Bmatrix}^{n+1} = \mathbf{G}\begin{Bmatrix} \phi \\ \eta \end{Bmatrix}^{n} + \begin{Bmatrix} \mathbf{0} \\ \mathbf{f} \end{Bmatrix}^{n}, \tag{20}$$

where $\mathbf{G}$ is a $2m \times 2m$ matrix consisting of kinematic and dynamic free surface boundary conditions and depends on the difference scheme adopted, m represents the number of sources distributed above or over the free surface and $\mathbf{f}$ is an m-component forcing function column which plays no role in stability analysis and will be omitted hereinafter. Similar to the formation of equations (10)–(12), the explicit Euler scheme gives the matrix $\mathbf{G}$

$$\mathbf{G} = \begin{bmatrix} \mathbf{I} & -g\Delta t\mathbf{I} \\ \Delta t\mathbf{C}^* & \mathbf{I} \end{bmatrix}, \tag{21}$$

the implicit Euler scheme yields the matrix $\mathbf{G}$

$$\mathbf{G} = \begin{bmatrix} \mathbf{I} & g\Delta t\mathbf{I} \\ -\Delta t\mathbf{C}^* & \mathbf{I} \end{bmatrix}^{-1} \tag{22}$$

and the E–I Euler scheme produces the matrix $\mathbf{G}$

$$\mathbf{G} = \begin{bmatrix} \mathbf{I} & g\Delta t\mathbf{I} \\ \mathbf{0} & \mathbf{I} \end{bmatrix}^{-1} \begin{bmatrix} \mathbf{I} & \mathbf{0} \\ \Delta t\mathbf{C}^* & \mathbf{I} \end{bmatrix}, \tag{23}$$

where the submatrix $\mathbf{I}$ is an $m \times m$ identity matrix and the $m \times m$ submatrix $\mathbf{C}^*$ results from the influence coefficient matrix of the discretization system which is obtained from the Eulerian boundary element method.

4. APPLICATION OF MATRIX STABILITY ANALYSIS

A linearized system representing non-linear free surface problems has a large number of parameters of interest, which increases the complexity of a stability analysis. To circumvent this difficulty, we limit our attention to a particular class of parameters. Through the use of several applications, the usefulness of the stability analyses delineated previously is demonstrated.

4.1. Stability analysis for the desingularized method

The desingularized distance plays an important role in the numerical stability of this method. In this subsection we first try to set up the stability criterion for the desingularized distance by using the above stability analysis. For simplicity we consider a simple case with a unit source distributed above the origin at a distance d and a field point located at the origin. By applying the E–I Euler scheme, the necessary stability conditions for the desingularized distance d are given by the inequalities

$$-4 \leqslant g\Delta t^2/d \ln d \leqslant 0 \quad \text{and} \quad -4 \leqslant -g\Delta t^2/d \leqslant \mathbf{0} \tag{24}$$

for two-dimensional and three-dimensional cases respectively; see Reference 11 for details.

Based upon the desingularized boundary element method, the discrete set of equations (3) and (4) can be rewritten as

$$\begin{Bmatrix} \phi_{\mathscr{D}} \\ \partial\phi_{\mathscr{N}}/\partial\mathbf{n} \end{Bmatrix} = \mathbf{C}\begin{Bmatrix} \sigma_{\mathscr{D}} \\ \sigma_{\mathscr{N}} \end{Bmatrix}. \tag{25}$$

By deriving the Fredholm integral equation of the first kind from equations (1) and (2),[12,13] the above system of equations can be further rewritten as

$$\begin{Bmatrix} \partial\phi_{\mathscr{D}}/\partial\mathbf{n} \\ \partial\phi_{\mathscr{N}}/\partial\mathbf{n} \end{Bmatrix} = \mathbf{C}' \begin{Bmatrix} \sigma_{\mathscr{D}} \\ \sigma_{\mathscr{N}} \end{Bmatrix}. \tag{26}$$

Substituting equations (25) into equations (26) and withdrawing the N_f-component subvector related to the free surface from the above system yields

$$\left\{\frac{\partial\phi_{\mathscr{D}}}{\partial\mathbf{n}}\right\}N_f = \mathbf{C}'_{N_f\times N}\mathbf{C}^{-1}_{N\times N}\begin{Bmatrix} \phi_{\mathscr{D}} \\ \partial\phi_{\mathscr{N}}/\partial\mathbf{n} \end{Bmatrix}_N = \mathbf{C}^*\{\phi_{\mathscr{D}}\}_{N_f} + \{\mathbf{f}\}_{N_f}, \tag{27}$$

where N_f is the number of sources distributed above the free surface and N is the total number of sources.

The matrix method is of special interest because of its ability to investigate numerical stability without extensive simplification. Here we will directly use the matrix method developed in Section 3 to study the numerical properties of the desingularized boundary element method. For the E–I Euler scheme the matrix **G** takes the form

$$\mathbf{G} = \begin{bmatrix} \mathbf{I} & g\Delta t\mathbf{I} \\ \mathbf{0} & \mathbf{I} \end{bmatrix}^{-1}\begin{bmatrix} \mathbf{I} & \mathbf{0} \\ \Delta t\mathbf{C}^* & \mathbf{I} \end{bmatrix}. \tag{28}$$

Here we use the above equation to investigate the sloshing of waves in a tank ($L=4$ and $H=1$), the objective being to determine the stable ranges of desingularized distance d. Figure 2 provides the numerical stability analysis for the 4×1 sloshing tank where the number of panels is equal to $40\times 10\times 10$, $\Delta x = 0{\cdot}1$ and $\Delta t = 0{\cdot}05, 0{\cdot}1, 0{\cdot}3$ and $0{\cdot}35$. The stable ranges of desingularized distance d are determined by the largest moduli of eigenvalues, $|\lambda|_{\max}$ versus l_d, where the desingularization factor is defined as $l_d = d/\Delta x$. Taking $\nu = 1$ in equation (5), we have that the results provided in Figure 2 are in fair agreement with the numerical experiments provided by Cao.[7] Furthermore, when $\Delta t > 0{\cdot}35$, there is no stable range of desingularized distance for this certain condition. Figure 3 shows the effect of desingularized distance on the *non-linear* numerical simulations of sloshing waves. The results show the free surface elevations at the midpoint of the sloshing tank, where $l_d = 0{\cdot}5$ lies in the unstable range, $l_d = 1{\cdot}05$ is near the critical point and $l_d = 3{\cdot}0$ is seated in the stable range. It should be pointed out that large mesh and time step sizes were adopted to demonstrate the characteristics of numerical stability and hence some size effects in the form of wave beating could be observed. Usually there are significant size effects on the larger-amplitude case and insignificant size effects on the smaller-amplitude case. Here the non-dimensionalization is achieved by taking $g = 1$ in the numerical simulation. Calculations were performed on an HP735 workstation with single-precision accuracy.

From stability analysis we know that the E–I Euler scheme is conditionally neutrally stable and the explicit Euler scheme is unconditionally unstable. Figure 4 gives examples that show the time step effects on the explicit Euler scheme. Here the desingularized method with the explicit Euler scheme and $d = 3\Delta x$, i.e. $l_d = 3$, is applied to simulate the non-linear sloshing of waves over period without using any regridding technique. The initial conditions are defined so that the free surface at $t = 0$ is at rest and takes a sinusoidal form as an initial wave elevation. Three different time steps, i.e. $\Delta t = 0{\cdot}01, 0{\cdot}1$ and $0{\cdot}2$ with $|\lambda|_{\max} = 1{\cdot}0018, 1{\cdot}1629$ and $1{\cdot}5523$ respectively, are adopted here to demonstrate the time step effects on the numerical simulations of sloshing waves. The sloshing tank used here is 4×1, as illustrated in Figure 5. Figure 4 also suggests that by careful selection of numerical parameters such as time step and mesh size, schemes that are marginally unstable in a

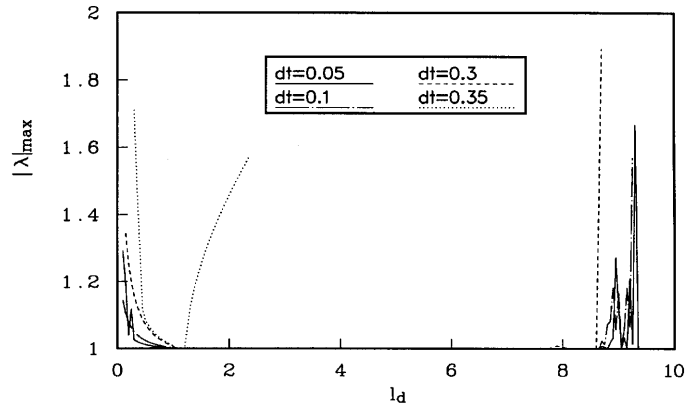

Figure 2. Stable range of desingularized distance (E–I Euler method)

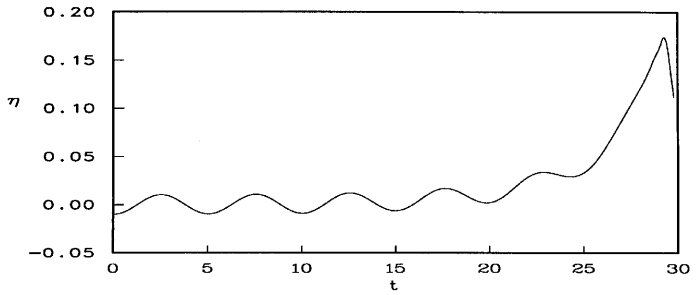

(a) *E-I* Euler method (Case: $dt = 0.1$, $dx = 0.1$, $l_d = 0.5$)

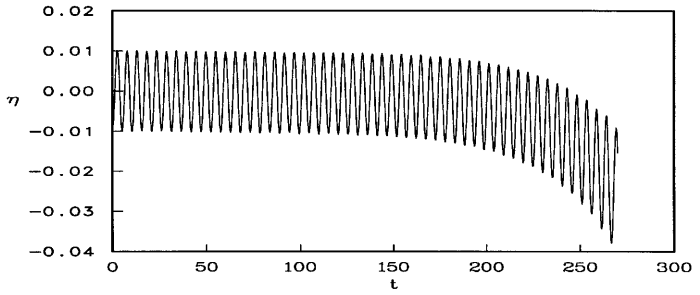

(b) *E-I* Euler method (Case: $dt = 0.1$, $dx = 0.1$, $l_d = 1.05$)

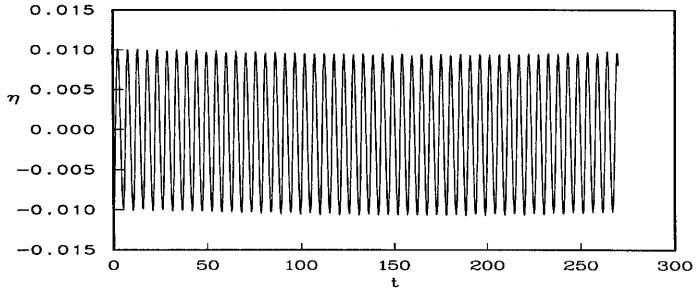

(c) *E-I* Euler method (Case: $dt = 0.1$, $dx = 0.1$, $l_d = 3.0$)

Figure 3. Effect of desingularized distance on simulations of sloshing waves

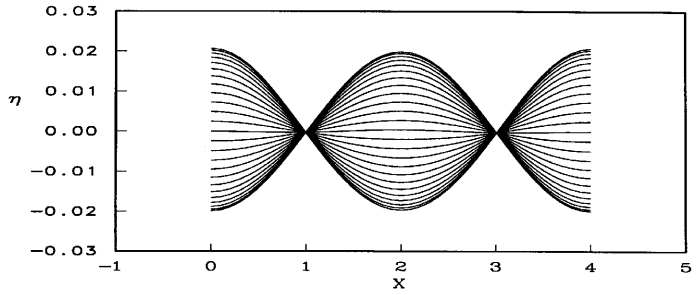

(a) Explicit Euler method ($\Delta t = 0.01$, $\Delta x = 0.1$, $|\lambda|_{max} = 1.0018$)

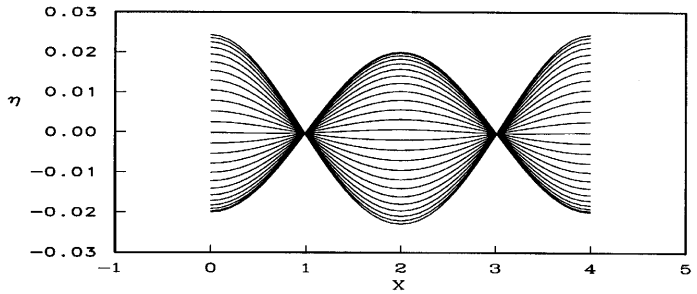

(b) Explicit Euler method ($\Delta t = 0.1$, $\Delta x = 0.1$, $|\lambda|_{max} = 1.1629$)

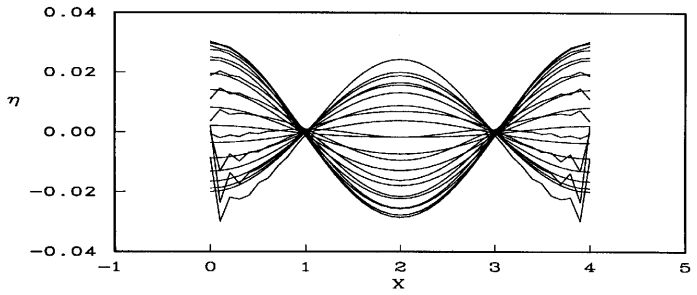

(c) Explicit Euler method ($\Delta t = 0.2$, $\Delta x = 0.1$, $|\lambda|_{max} = 1.5523$)

Figure 4. Stability of sloshing wave elevation over one period

linear sense sometimes give satisfactory results for short-time non-linear simulations. This may help explain the popularity of explicit methods in mixed non-linear E–I schemes.

Conservation of mass and energy plays a significant role in the stability of numerical schemes. Figure 6 demonstrates the conservation of energy, including kinetic energy and potential energy, where the theoretical total energy comes from the linear wave theory. Because this is a small-

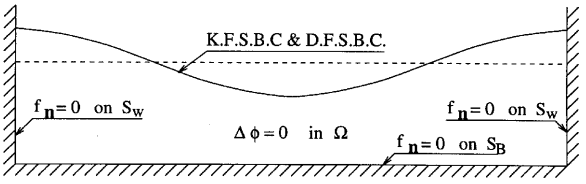

Figure 5. Schematic sloshing tank (4 × 1)

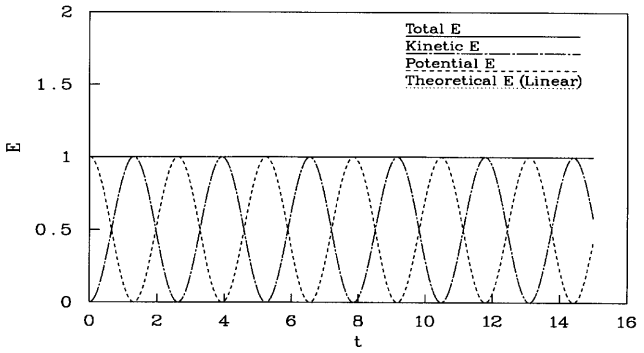

Figure 6. Energy (E) conservation (E–I Euler scheme, $\Delta t = 0{\cdot}01$, $\Delta x = 0{\cdot}1$, $|\lambda|_{\max} = 1{\cdot}01$)

amplitude sloshing wave, i.e. $A = 0{\cdot}02$, the numerical result shows good agreement with the linear theory. Figure 7 illustrates the time step effects on conservation of energy. This figure shows that a large time step has significant effects on conservation of energy, where the numerical results are normalized by total energy. To some extent both the E–I and explicit Euler schemes violate the

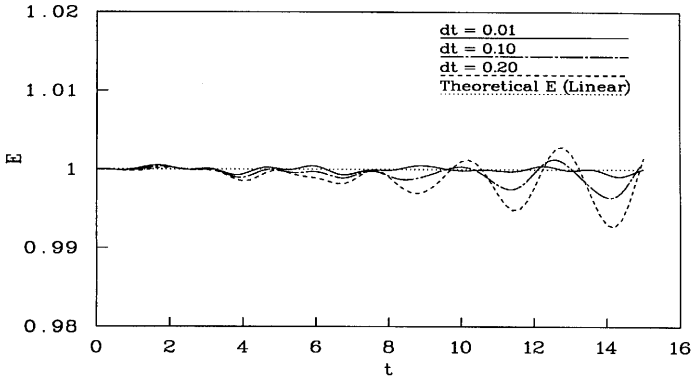

(a) *E-I* Euler scheme ($\Delta x = 0.1$, $|\lambda|_{max} = 1.0$)

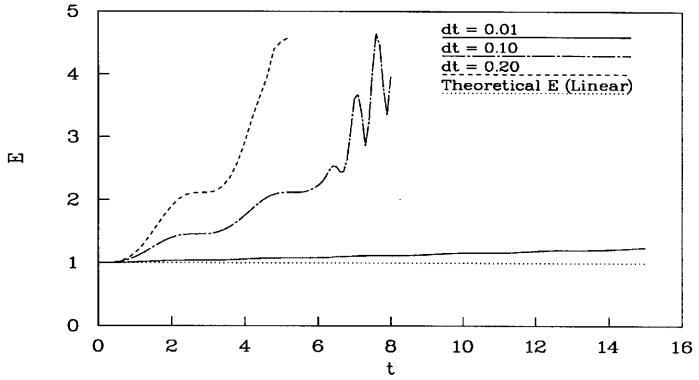

(b) Explicit Euler scheme ($\Delta x = 0.1$, $|\lambda|_{max} = 1.0018, 1.1629, 1.5523$)

Figure 7. Time step effects on energy (E) conservation

conservation of energy for neutrally stable and marginally unstable conditions. Generally speaking, the neutrally stable E–I Euler scheme is significantly better than the unstable explicit Euler scheme, especially in long-time non-linear simulation.

4.2. Stability analysis for the source–doublet method

Here we apply the matrix method to the stability analysis for the source–doublet panel method. Applying a simple Euler scheme to the kinematic boundary condition yields

$$\mathbf{x}_{\mathrm{f}}^{n+1} = \mathbf{x}_{\mathrm{f}}^{n} + \Delta\tau\mathbf{v}, \tag{29}$$

where the z-component of $\mathbf{x}_{\mathrm{f}}$, together with the square of the perturbation velocity, allows evaluation of the gradient of the potential with respect to time from the Bernoulli equation

$$\frac{\mathrm{D}\phi}{\mathrm{D}\tau} = \frac{1}{2}\left(\frac{\eta}{Fr^2} - v^2\right), \tag{30}$$

where Fr is the Froude number given by $V_{\mathrm{REF}}/\sqrt{(gL_{\mathrm{REF}})}$. Then applying a Euler scheme to the above equation provides the new doublet distribution on the free surface for the next time step, i.e.

$$\mu^{n+1} = \mu^{n} + \frac{1}{4\pi}\Delta\tau\phi. \tag{31}$$

It should be pointed out that the source–doublet panel method[10] adopts an explicit Euler scheme at the intersection point, an E–I Euler scheme at the far-field boundary and an average Euler scheme all over the free surface by using a weight function related to the distance between the field point and the intersection point.

Similar to the formation of equations (21)–(23), applying a different Euler schemes yields the following equations. The explicit Euler scheme gives the matrix $\mathbf{G}$

$$\mathbf{G} = \begin{bmatrix} \mathbf{I} & (\Delta\tau/8\pi Fr^2)\mathbf{I} \\ 4\pi\Delta\tau\mathbf{C}^* & \mathbf{I} \end{bmatrix}; \tag{32}$$

the implicit Euler scheme yields the matrix $\mathbf{G}$

$$\mathbf{G} = \begin{bmatrix} \mathbf{I} & -(\Delta\tau/8\pi Fr^2)\mathbf{I} \\ -4\pi\Delta\tau\mathbf{C}^* & \mathbf{I} \end{bmatrix}^{-1} \tag{33}$$

and the E–I Euler scheme produces the matrix $\mathbf{G}$

$$\mathbf{G} = \begin{bmatrix} \mathbf{I} & -(\Delta\tau/8\pi Fr^2)\mathbf{I} \\ \mathbf{0} & \mathbf{I} \end{bmatrix}^{-1} \begin{bmatrix} \mathbf{I} & \mathbf{0} \\ 4\pi\Delta\tau\mathbf{C}^* & \mathbf{I} \end{bmatrix}, \tag{34}$$

where the submatrix $\mathbf{I}$ is an $N_{\mathrm{f}} \times N_{\mathrm{f}}$ identity matrix and the $N_{\mathrm{f}} \times N_{\mathrm{f}}$ submatrix $\mathbf{C}^*$ results from the matrix of influence coefficients calculated by the USAERO/FSP code.

To obtain the submatrix $\mathbf{C}^*$, rewriting equation (6) in matrix form yields

$$[C]\{\mu\} + [B]\{\sigma\} = 0, \tag{35}$$

where $[C]$ and $[B]$ are $N \times N$ matrices and $\{\mu\}$ and $\{\sigma\}$ are N column vectors. Here $N = N_{\mathrm{f}} + N_{\mathrm{b}}$ is the total panel number. Equation (35) can be further rewritten as

$$\{\mu\} = -[C]^{-1}[B]\{\sigma\} = [A]\{\sigma\}, \tag{36}$$

where the matrix $[A]$ is given by USAERO/FSP. Currently, USAERO/FSP has only one option to output the matrix of influence coefficients, which is the direct solver. The solution provides the

doublet values on the hull panels and the source values on the free surface panels. Thus equation (36) gives

$$\begin{Bmatrix} \sigma_{N_b} \\ \sigma_{N_f} \end{Bmatrix} = \begin{bmatrix} \mathbf{A_{11}} & \mathbf{A_{12}} \\ \mathbf{A_{21}} & \mathbf{A_{22}} \end{bmatrix}^{-1} \begin{Bmatrix} \mu_{N_b} \\ \mu_{N_f} \end{Bmatrix} = \begin{bmatrix} \mathbf{C}^*_{11} & \mathbf{C}^*_{12} \\ \mathbf{C}^*_{21} & \mathbf{C}^* \end{bmatrix} \begin{Bmatrix} \mu_N \mathbf{b} \\ \mu_{N_f} \end{Bmatrix}, \tag{37}$$

where the submatrix $\mathbf{C}^*$ is the $N_f \times N_f$ matrix which gives

$$\{\sigma\}_{N_f} = [\mathbf{C}^*]\{\mu\}_{N_f}. \tag{38}$$

The dominant diagonal terms of the coefficient submatrix $\mathbf{C}^*$ always have negative values. This differs from when we use the desingularized method, where the dominant diagonal terms of $\mathbf{C}^*$ always have positive values. This is because the notation used in the source–doublet panel method is opposite from that adopted for the desingularized method.

The stability analyses of non-linear numerical simulations for cases of interest will be provided next. First we study the stability characteristics of different Euler schemes for a flared body undergoing forced sinusoidal vertical motion. The body geometry is shown in Figures 8 and 10. Based on the conditions of experimental 'Run 25', i.e. frequency $f = 0{\cdot}598$ Hz and moderate amplitude $A = 1{\cdot}257$ in (see Reference 11 where the complete experimental test matrix and results are described), a numerical simulation was conducted by USAERO/FSP which sets up a pseudo-axisymmetric condition where a segment of the body geometry and free surface is constructed with a 10° wedge angle. The code was instructed to perform an azimuthal sum of 36 identical strength panels for each influence coefficient (see Figure 8). This treatment is to save computer time. For the purpose of stability analysis, here equations (32)–(34) are used to investigate the deck wetness case, experimental run 25, where the numbers of panels on the flared body and on the free surface are 12 and 28 respectively and $\Delta t = 0{\cdot}01$. The far-field open boundary was set at four body diameters away from the Z-axis. The distribution of the 80 complex eigenvalues relative to the unit circle given in Figure 9 shows that the explicit scheme is unstable where $|\lambda|_{\max} = 1{\cdot}00213456$, the E–I scheme is neutrally stable where $|\lambda|_{\max} = 1{\cdot}0$ and the implicit scheme is stable where $|\lambda|_{\max} = 0{\cdot}999980092$. We have the same conclusion as that predicted in Reference 11 for the simple stability analysis.

The stability characteristics of free drop tests have also been investigated here. The free drop body entry into initially calm water is described in Reference 11. The isometric view of the flared body is shown in Figure 10; see Reference 11 for its offsets. Similar to above, a pseudo-axisymmetric

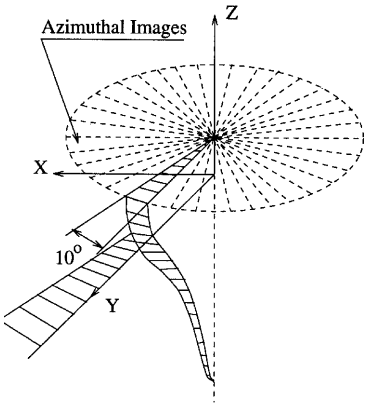

Figure 8. Co-ordinate systems and azimuthal segments

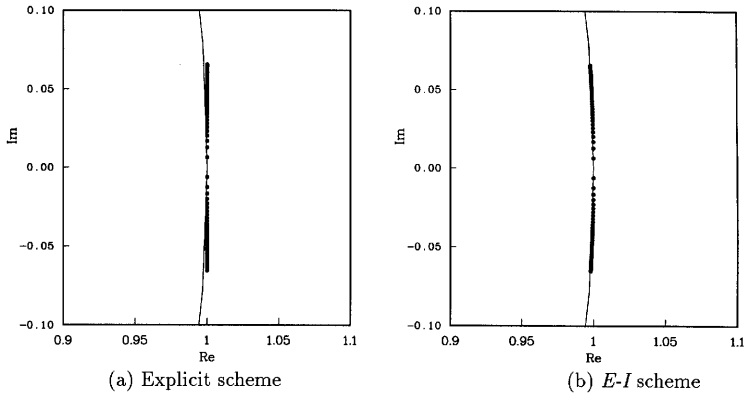

(a) Explicit scheme (b) *E-I* scheme

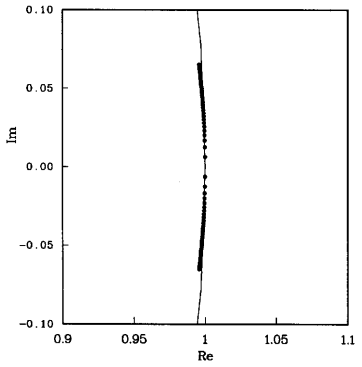

(c) Implicit scheme

Figure 9. Eigenvalue distribution in complex plane, run 25

condition is set up where a segment of the body geometry and free surface is constructed with a 10° wedge angle. Figure 8 gives the details of the co-ordinate systems and azimuthal segments. Figure 11 demonstrates the time step size effect on the numerical simulations for the case of dropping height $h = 2$ ft (0·61 m), where three different time step sizes are taken, i.e. $\Delta t = 0{\cdot}00102, 0{\cdot}001531$ and 0·003072 s. The vertical slamming coefficient C_{vs} was defined in Reference 17 as

$$C_{vs} = 2m\ddot{z}/\rho\pi L^2 V_0^2, \tag{39}$$

where m is the mass, $\ddot{z}$ is the vertical acceleration, ρ is the water density, L is a reference length equal to the radius of the top circle of the cusped body, i.e. 7·8 in (19·8 cm), and V_0 is the initial vertical impact velocity described above. Other results are also presented in non-dimensional forms[17] where the vertical acceleration and velocity are normalized by the gravity acceleration g and V_0 respectively. Time is non-dimensionalized by $V_0/2L$. Bottom and flare impacts are highly non-linear phenomena. The numerical simulation is very sensitive to the time step size, whose stable range is very small. From Figure 11 we know that only $\Delta t = 0{\cdot}001531$ s yields reasonably good results. The smallest time step $\Delta t = 0{\cdot}00102$ s caused termination of the simulation too early owing to dispersion. The largest time step $\Delta t = 0{\cdot}003072$ shows the largest dissipative error, so that the simulation is also forced to stop. In the simulations we took 22 panels on the body and 38 panels on the free surface. Table I lists maximum moduli of eigenvalues for three different Euler schemes. When $\Delta t = 0{\cdot}00102$ and 0·001531 s, the maximum moduli of the eigenvalues of the implicit scheme are equal to unity

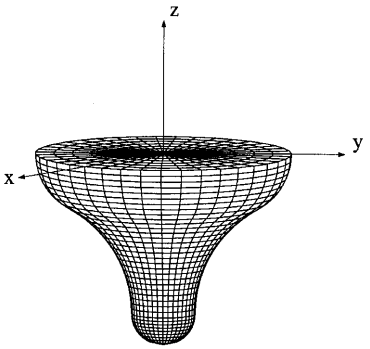

Figure 10. Schematic diagram of co-ordinate systems and geometry of body

instead of less than unity as we had seen before. This is because of round-off error for such small time step sizes.

4.3. Effect of artificial damping

Artificial absorption devices were originally devised to provide improvements in minimizing wave reflections, which has been discussed before. As an additional benefit, this design can also be used to damp out the dispersive effect of numerical schemes. Israeli and Orszag[16] pointed out that there exists an *optimum* value of the cooling strength for maximum wave absorption; nevertheless, how to

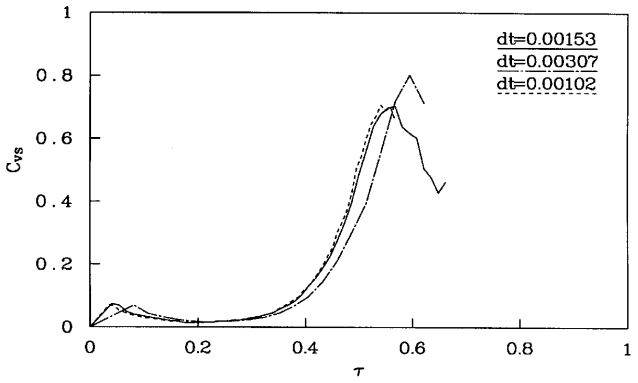

Figure 11. Stability analysis of free drop test simulations (source–doublet method (USAERO/FSP), $h = 2$ ft)

Table I. Maximum moduli for free drop test with $h = 2$ ft

Time step size Δt (s)	Explicit scheme $\lvert\lambda\rvert_{max}$	E–I scheme $\lvert\lambda\rvert_{max}$	Implicit scheme $\lvert\lambda\rvert_{max}$
0·003067	1·00000262	1·0	0·999999940
0·001533	1·00000060	1·0	1·0
0·001022	1·00000024	1·0	1·0

determine this optimum value is not straightforward. Nakos *et al.*[6] attempted to use their spectral stability analysis to investigate some absorption devices without giving specific values of Newtonian cooling coefficients. In this subsection we will use the matrix method to determine ranges of the Newtonian cooling strength v_0 for the purpose of numerical stability, thus bounding the optimum value for the Newtonian cooling strength.

A linearizing artificial absorption system for the non-linear model given by equation (7) can be expressed as

$$\phi_t = -gz - v\phi_z, \tag{40}$$

$$\eta_t = \phi_z. \tag{41}$$

Using the E–I Euler scheme yields the matrix **G** taking the form

$$\mathbf{G} = \begin{bmatrix} \mathbf{I} & (g\Delta t + v)\mathbf{I} \\ \mathbf{0} & \mathbf{I} \end{bmatrix}^{-1} \begin{bmatrix} \mathbf{I} & v\mathbf{I} \\ \Delta t\mathbf{C}^* & \mathbf{I} \end{bmatrix}, \tag{42}$$

where the Newtonian cooling is defined by

$$v(x) = \begin{cases} 0, & 0 \leqslant x \leqslant x_0, \\ v_0\left[1 - \cos\left(\pi \dfrac{x - x_0}{L - x_0}\right)\right], & x_0 < x \leqslant L. \end{cases} \tag{43}$$

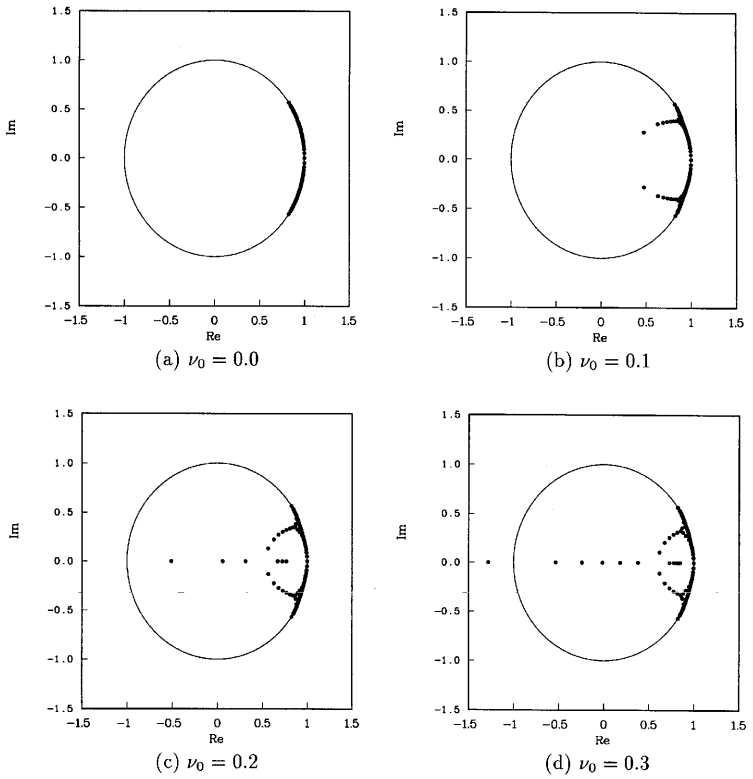

Figure 12. Eigenvalue distribution in complex plane

This function and its first derivative have zero values at $x = x_0$, thus minimizing the wave reflection of the absorption device.

Figure 12 illustrates the eigenvalue distribution in the complex plane due to variation of the Newtonian cooling strength v_0 from 0·0 to 0·3. The specific example is a tank with an absorber at one end. The results tell us that the larger the Newtonian cooling strength v_0, the more influence over the numerical system the artificial damping device has. However, when $v_0 = 0{\cdot}3$, one of the eigenvalues is greater than unity, thus predicting that the corresponding non-linear simulation may eventually be spoiled by numerical instability. The overdamping effect not only does not stabilize the numerical system but also causes the instability of the system. In summary, for the sloshing case considered, the results of the cooling strength predicted by the matrix stability analysis lie between 0·0 and 0·3.

Numerical stability analyses were performed based on a 6×1 sloshing tank, i.e. $L = 6$ and $H = 1$, where the number of panels is equal to $60 \times 10 \times 10$, $\Delta x = 0{\cdot}1$, $\Delta t = 0{\cdot}1$ and the absorbing beach starts at $x_0 = 4$, i.e. $4 < x \leqslant 6$. The E–I Euler scheme given by equation (42) is applied to analyse the stability. From Reference 11 we know that most of the normal modes have zero value over the absorbing beach. From the node superposition principle, if those modes play a significant role in the wave elevation, the absorption devices achieves the desired results. Figure 13 shows the comparison of the normal modes η between two different devices, i.e. $v = v_0\{1 - \cos[\pi(x - x_0)/(L - x_0)]\}$ and $v = v_0\{1 + \cos[\pi(x - x_0)/(L - x_0)]\}$, where the latter and its first derivative have non-zero values at

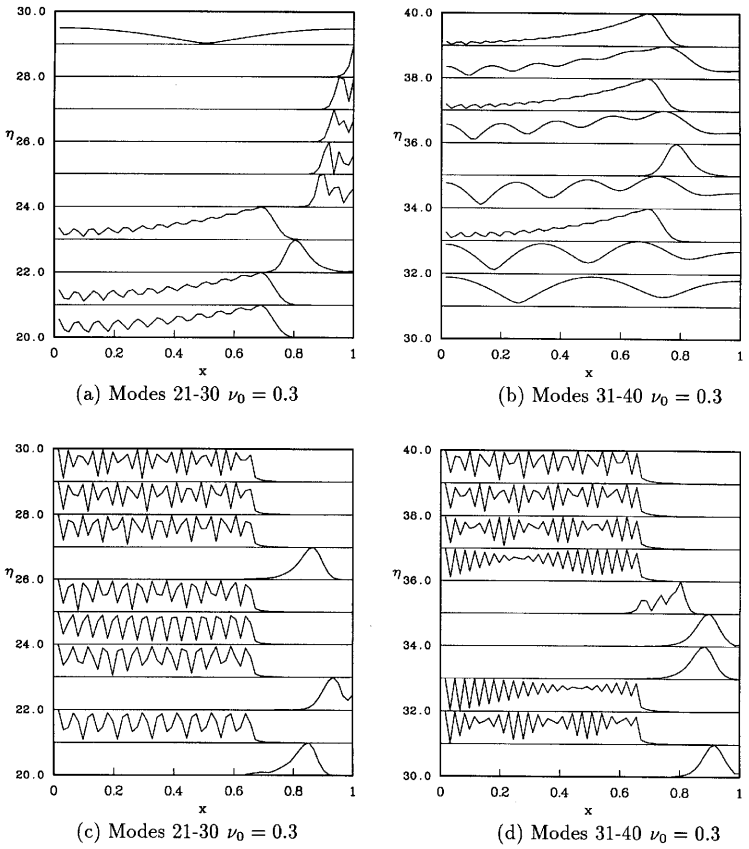

(a) Modes 21-30 $\nu_0 = 0.3$ (b) Modes 31-40 $\nu_0 = 0.3$

(c) Modes 21-30 $\nu_0 = 0.3$ (d) Modes 31-40 $\nu_0 = 0.3$

Figure 13. Comparison between (a, b) $v = v_0\{1 - \cos[\pi(x - x_0)/(L - x_0)]\}$ and (c, d) $v = v_0\{1 + \cos[\pi(x - x_0)/(L - x_0)]\}$

$x = x_0$. Figure 13 shows that the latter device, i.e. (c) and (d), has high-wave-number modes compared with the former device, i.e. (a) and (b). When short-wave modes play a major role in determining the wave elevation, the result may be spoiled by numerical dispersion associated with improperly selected absorption devices.

To further understand the mechanism of absorption devices, Figures 14 and 15 are used to illustrate the artificial damping effect on simulations of sloshing waves which correspond to the four cases shown in Figure 12, i.e. $v_0 = 0{\cdot}0, 0{\cdot}1, 0{\cdot}2$ and $0{\cdot}3$. The numerical simulations provided in Figures 14 and 15 show good agreement with Figure 12, where the case $v_0 = 0{\cdot}3$ shows that the simulation finally stopped at the time equal to 88 owing to overdamping and the associated numerical instability. This example strongly suggests that when we design an absorption device, we have to be careful not to unknowingly overdamp.

5. CONCLUSIONS

This research presents a systematic methodology of numerical stability for the study of numerical properties of mixed Eulerian–Lagrangian schemes for the numerical simulation of non-linear free surface flows. Two different numerical schemes, i.e. a source–doublet panel method and a desingularized method, are investigated. The matrix stability method is applied in establishing stability criteria as well as evaluating the effects of the desingularized distance and the artificial

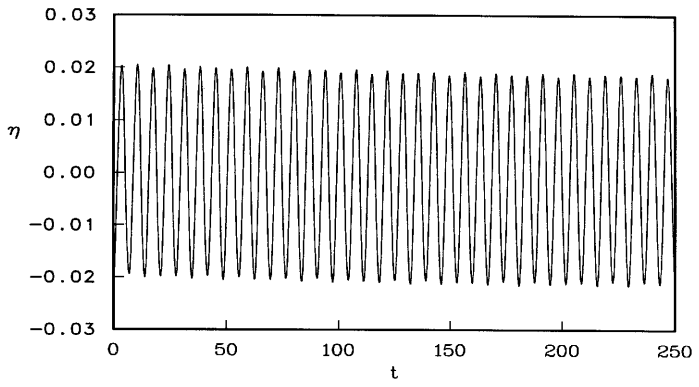

(a) $\nu_0 = 0.0$

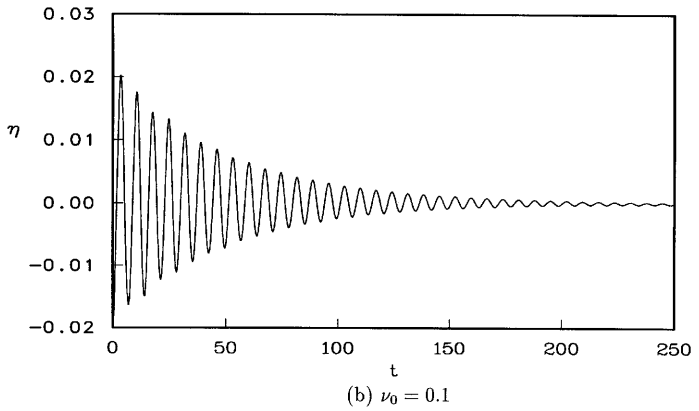

(b) $\nu_0 = 0.1$

Figure 14. Artificial damping effect on simulations of sloshing waves

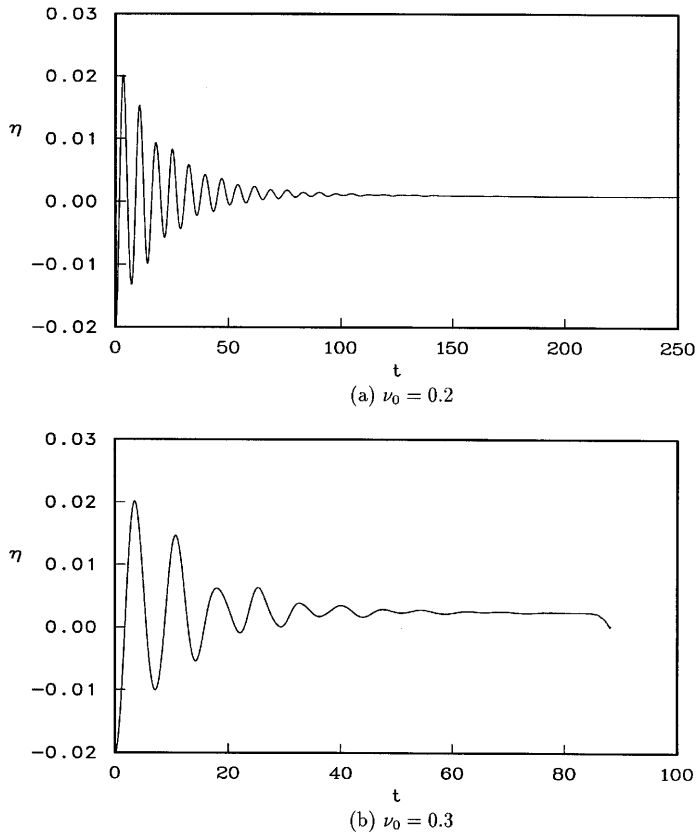

Figure 15. Artificial damping effect on simulations of sloshing wave

absorption device, thus expounding the role stability analysis plays in the success of the numerical method, remedying its shortcomings and extending its applicability. Examples considered illustrate the usefulness of this stability analysis. This study shows that the neutrally stable scheme or the weakly dissipative scheme is ideal in long-time simulations of non-linear free surface problems.

ACKNOWLEDGEMENTS

The authors would like to give special thanks to Dr. Brian Maskew of Analytical Methods, Inc. for providing programme USAERO/FSP. This research has been supported by the Office of Naval Research, United States Navy under contracts DOD-G-N00014-90-J-1818, DOD-G-N-00014-94-1-0652 and DOD-G-N00014-96-1-0482 with programme managers Jim Fein, Dr. Peter Majumdar and Dr. Edwin Rood respectively.

REFERENCES

1. M. S. Longuet-Higgins and C. D. Cokelet, 'The deformation of steep surface waves on water: I. A numerical method of computation', *Proc. R. Soc. Lond. A*, **350**, 1–26 (1976).
2. R. W. Yeung, 'Numerical methods in free-surface flows', *Ann. Rev. Fluid Mech.*, **14**, 395–442 (1982).

3. P. D. Sclavounos and D. E. Nakos, 'Stability analysis of panel methods for free-surface flows with forward speed', *Proc. 17th Symp. on Naval Hydrodynamics*, 1988, National Academy Press, Washington, D.C. 1989, pp. 29–48.
4. J. H. Park and A. W. Troesch, 'Numerical modeling of short-time scale nonlinear water waves generated by large vertical motions of non-wallsided bodies', *Proc. 19th Symp. on Naval Hydrodynamics*, Seoul, 1992, National Academy Press, Washington, D.C., 1994, pp. 115–130.
5. D. G. Dommermuth, D. K. Yue, W. M. Lin and R. J. Rapp, 'Deep water plunging breakers: a comparison between potential theory and experiments', *J. Fluid Mech.*, **189**, 423–442 (1988).
6. D. E. Nakos, D. C. Kring and P. D. Sclavounos, 'Rankine panel methods for transient free surface flows', *Proc. 6th Int. Conf. on Numerical Ship Hydrodynamics*, Iowa City, 1993, National Academy Press, Washington, D.C., 1994.
7. Y. S. Cao, 'Computations of nonlinear gravity waves by a desingularized boundary integral method', *Ph.D. Thesis*, Department of Naval Architecture and Marine Engineering, University of Michigan, Ann Arbor, MI, 1991.
8. Y. S. Cao, W. W. Shultz and R. F. Beck, 'A three-dimensional desingularized boundary integral method for potential problems', *Int. j. numer methods fluids*, **11**, 785–803 (1991).
9. Y. S. Cao, R. F. Beck and W. W. Schultz, 'Numerical computations of two-dimensional solitary waves generated by moving disturbances', *Int. j. numer methods fluids*, **17**, 905–920 (1993).
10. B. Maskew, 'USAERO/FSP: a time-domain approach to complex free-surface problems', *Proc. Symp. on High-Speed Marine Vehicles*, Naples, 1991 Naval Studies Board, Washington, D.C., 1992.
11. M. L. Wang, 'A study of fully nonlinear free surface flws', *Ph.D. Thesis*, Department of Naval Architecture and Marine Engineering, University of Michigan, Ann Arbor, MI, 1995.
12. H. Lamb, *Hydrodynamics*, Dover, New York, 1932.
13. C. C. Mei, *The Applied Dynamics of Ocean Surface Waves*, World Scientific, Singapore, 1992.
14. B. Maskew, 'Program VSAERO theory document', *NASA CR-4023*, 1987.
15. A. Sommerfeld, *Partial Differential Equations in Physics*, Academic, New York, 1949.
16. M. Israeli and S. A. Orszag, 'Approximation of radiation boundary conditions', *J. Comput. Phys.*, **41**, 115–135 (1981).
17. A. W. Troesch and C. G. Kang, 'Hydrodynamic impact loads on three-dimensional bodies', *Proc. 16th Symp. on Naval Hydrodynamics*, Berkeley, CA, 1986, National Academy Press, Washington, D.C., 1987, pp. 537–558.

